



Numerical modeling of turbulence and its effect on ocean current turbines



Parakram Pyakurel ^{a,*}, James H. VanZwieten ^a, Manhar Dhanak ^a, Nikolaos I. Xiros ^b

^a Florida Atlantic University, Boca Raton, FL, USA

^b University of New Orleans, New Orleans, LA, USA

ARTICLE INFO

Article history:

Received 22 April 2016

Revised 18 October 2016

Accepted 11 January 2017

Available online 12 January 2017

Keywords:

Turbulence

Inertial subrange

Ocean current turbine

Kolmogorov's 5/3 law

Turbulence intensity

Hydrokinetic power

ABSTRACT

An approach for numerically representing turbulence effects in the simulation of ocean current turbines (OCT)s is described. Ambient turbulence intensity and mean flow velocity are utilized to develop analytic expressions for flow velocities at a grid of nodes that are a function of time. This approach is integrated into the numerical simulation of an OCT to evaluate effects of turbulence on performance. For a case study a moored OCT with a 20 m rotor diameter is used. Mean power in the presence of ambient turbulence intensities (TIs) of 5% and 20% are found to be 370 kW and 384 kW, with standard deviations of 17.2 kW and 74.6 kW respectively. Similarly, the axial loads on a single blade of the three-bladed rotor are found to be 139 kN and 140 kN, with standard deviations of 3 kN and 12 kN respectively for these TIs.

© 2017 Elsevier Ltd. All rights reserved.

1. Introduction

Ocean currents represent a significant source of marine hydrokinetic energy that may be harnessed and converted to electricity using ocean current turbines (OCT)s [1]. Based on the HYbrid Coordinate Ocean Model (HYCOM) model [2], ocean currents occur over a total area of 836,000 km² worldwide with average energy densities greater than 0.5 kW/m² at a depth of 50 m [3]. In the US, electricity production based on ocean currents has a technically extractable potential of 163 TWh/year [4], which is equivalent to 4% of 2014 US electricity production [5]. Off Florida, the time-averaged ocean current energy density can exceed 3.0 kW/m² [6]. Prototype OCTs have been developed to harness this resource and tested offshore [7]. Research and development of OCTs is also being carried out with the goal of producing power from the Kuroshio Current off Japan and Taiwan [8].

Turbulence causes fatigue loadings on these devices and longitudinal turbulence has been found to be a primary fatigue load driver for horizontal-axis tidal turbines [9]. Ambient turbulence is also found to impact the wake profile produced by the turbines [10,11]. Since wake propagation characteristics will affect the velocity experienced by downstream turbines in an OCT farm, turbulence plays an important role in optimization of the turbine layout on the farm.

The simulation tool TurbSim was developed by National Renewable Energy Laboratory (NREL) to generate turbulent inflow simulations based on a given set of initial boundary conditions using ensemble statistics [12]. This tool treats turbulent flow velocity as a stationary signal that has a constant mean and standard deviation if the sampling period is sufficiently large. Spectra of velocity components and spatial coherence are defined in the frequency domain, and an inverse Fourier

* Corresponding author.

E-mail address: ppyakurel2014@fau.edu (P. Pyakurel).

transform is used to generate velocity time histories. The generated time history can then be integrated into the turbine simulation tool Aerodyn [13]. Thus, a time history of the flow field is created prior to running turbine simulations.

Marine turbines have been found to be most sensitive to turbulence with frequencies below about 1 Hz [14]. The frequencies where a turbine will have a strong response is therefore likely to fall within and also extend below the inertial subrange, which is generally accepted to be in the frequency range of 0.2 Hz to 2 Hz [15]. Inertial subrange is the part of the wave-number spectrum where the rate of energy transfer through the spectrum is dominant compared to the rate of supply and dissipation of turbulent energy [16]. Furthermore, energy is transferred from larger scale eddies to smaller scale eddies with negligible viscous dissipation [17]. Turbulence energy spectrum within the inertial subrange can be generalized to be inversely proportional to the 5/3 power of frequency [18]. Vertical flow motions at frequencies lower than 0.2 Hz in tidal areas of interest are likely suppressed due to the constraints in vertical excursions imposed by the shallow water depth of the region [15]. In water depths of 100 m + depth where an OCT may operate, these bottom boundary effects are not significant. Therefore, the flow structure will be more three-dimensional and the inertial range may extend to frequencies lower than 0.2 Hz. Furthermore, small scale turbulence, and in turn higher frequency components which also fall within inertial subrange, is known to interact directly with the shear layer bounding the turbine wake from the freestream flow [19]. For this reason, it is likely that in most cases the frequency range of interest may follow a -5/3 slope.

A numerical simulation created to predict performance of OCTs using an unsteady Blade Element Momentum (BEM) method has been developed by Southeast National Marine Renewable Energy Center (SNMREC) [20,21]. This unsteady BEM approach divides the annular stream tube into azimuthal sections to account for spatial velocity variations with time and allows calculation of turbine parameters such as power and axial force at every time step [22].

This paper presents a method for simulating turbulent flow that is primarily based on the research reported in [23,24]. The presented methodology allows turbulent flow velocities to be analytically expressed at each node on a spatial grid as a function of time, without having to generate entire velocity time history prior to running numerical simulations. This method is integrated into an OCT simulation code and the performance of the turbine is evaluated under different levels of turbulence.

2. Turbulence modeling in turbine simulation

In the BEM approach described in [20], the swept area of the turbine rotor is divided into annular and azimuthal sections to create a mesh grid, referred to in this paper as the “rotor grid,” over which water velocities are specified each time step at every node for calculating the hydrodynamic forces on the rotor. In the simulating flow described in [20], representative current shear and wave components of water velocities are generated. In this section, we describe how representative velocity components for turbulent flow may be generated such that they can be incorporated into the BEM model. In order to determine instantaneous velocities at every node on the rotor grid, the following parameters are needed as user inputs: mean flow speed \bar{U} , ambient turbulence intensity TI , minimum and maximum frequencies f_{min} and f_{max} associated with this TI , an along-flow coherence decay constant C , and factors P and Q that define the relationship between the standard deviations of velocity components (along-flow, across-flow and down directions). From these input parameters, expressions for velocities are obtained in frequency domain and then Fourier analysis is used to obtain analytic expressions for turbulent velocity perturbations as a function of time.

2.1. Velocity in frequency domain

This section defines the magnitudes of flow velocities for all three (along- and cross-flow) directions in frequency domain. A statistical method of simulating turbulence developed by Veers [23] is generally followed. However, in this paper the role of TI in determining the behavior of the frequency spectrum in the inertial range is considered. The details of the simulation approach when only a single component of velocity is available are described in [25]. Here, we extend the approach to incorporate all three components of velocity. Kolmogorov's 5/3 law [26] is presented to create an example spectra. However, if a better relationship between spectra and frequency is found, Eq. (1) can be replaced by a suitable expression while using the same approach discussed here without the loss of generality. Continuous power spectral density (PSD), $G(f)$, is calculated as a function of frequency, f , according to:

$$G(f) \propto f^{-\frac{5}{3}}, \quad (1)$$

which implies

$$G^m(f) = A_m f^{-\frac{5}{3}}, \quad (2)$$

where A_m is a constant for a given TI defined in Eq. (7); $m = u, v$ or w where u, v and w are velocity components in the along-flow (in the direction of the flow), across-flow (in compliance with the right hand coordinate system), and vertical (down) directions respectively; and $G^m(f)$ is corresponding one sided PSD.

The m component of standard deviation, σ_m , is related to $G^m(f)$ as [13]:

$$\sigma_m^2 = \int_{f_{\min}}^{f_{\max}} G^m(f) df. \quad (3)$$

The relationships among standard deviations are defined in this paper as $\sigma_u = P\sigma_u$ and $\sigma_w = Q\sigma_u$, where P and Q are constants that define the ratio between the standard deviation of the flow speed in the cross-flow and down directions over the standard deviation in the axial direction. Since TI and \bar{U} are also user inputs, it is convenient to express σ_u as:

$$\sigma_u = \frac{TI\bar{U}}{\sqrt{1 + P^2 + Q^2}}. \quad (4)$$

The TI can be expressed as [27]:

$$TI = \frac{|\sigma|}{|\bar{U}|}, \quad (5)$$

where σ is a vector containing the standard deviation of u , v and w ; \bar{U} is a vector containing the mean of u , v and w . The TIs associated with the three velocity components m , TI_m , are therefore given by:

$$TI_m = \frac{\sigma_m}{|\bar{U}|}, \quad (6)$$

It is noteworthy that $|\bar{U}| = \bar{U} = \sqrt{\bar{U}^2 + \bar{V}^2 + \bar{W}^2}$ where u , v and w are time averaged mean of u , v and w . To obtain an expression for A_m , Eq. (3) is integrated by incorporating Eqs. (2) and (6) in Eq. (3). The expression for A_m is thus:

$$A_m = \frac{2\bar{U}^2 TI_m^2}{3 \left[\frac{1}{f_{\min}^{\frac{2}{3}}} - \frac{1}{f_{\max}^{\frac{2}{3}}} \right]}. \quad (7)$$

Therefore, the continuous power spectral over the evaluated range can be written as:

$$G^m = \frac{2\bar{U}^2 TI_m^2}{3 \left[\frac{1}{f_{\min}^{\frac{2}{3}}} - \frac{1}{f_{\max}^{\frac{2}{3}}} \right]} f^{-5/3}, \quad (8)$$

assuming the TI is derived from this same frequency range. Examples with $f_{\min} = 0.01$ Hz and $f_{\max} = 1$ Hz are presented for $\bar{U} = 1.6$ m/s and $TI = 5\%$ and 20% in the Results section. Over this frequency range the associated spectra in the along stream direction for $P = 1$ and $Q = 1$ are $G_{5\%}^u = 6.92 \times 10^{-7} \times f^{-5/3}$ and $G_{20\%}^u = 0.0011 \times f^{-5/3}$ where subscripts of G indicate the associated TI .

To generate correlated components of water velocity over a fixed grid from the spectra as simulated flow, frequency discretization of spectra is carried out and a coherence function is defined. The continuous one sided PSD is discretized as in [23]:

$$\tilde{s}^m(\mathbf{f}) = G^m(f) \delta f, \quad (9)$$

where $\tilde{s}^m(\mathbf{f})$ is discretized PSD and δf is difference between consecutive frequencies. The boldface \mathbf{f} is used to denote that \mathbf{f} is a discretized mid-frequency vector with $\mathbf{f} = f_1, f_2, \dots, f_N$, where $N + 1$ is the total number of frequency discretization within f_{\min} to f_{\max} . The mid-frequency is the average of two consecutive frequencies obtained by discretizing f_{\min} to f_{\max} into N equal parts. For each velocity component, the flow between any two nodes i and j will be partially correlated with correlation decreasing as the distance between the nodes increases. A coherence function, Coh , defines the correlation between two nodes [23]:

$$Coh_{ij}(\mathbf{f}) = \exp\left(-\frac{C \Delta r_{ij} \mathbf{f}}{\bar{U}}\right), \quad (10)$$

where Δr_{ij} is distance between nodes i and j , and C is a coherence decay constant.

The discretized cross spectral density between nodes i and j , $\tilde{s}^m(\mathbf{f})$, related to this Coherence function is [23]:

$$\tilde{s}^m(\mathbf{f}) = Coh_{ij}(\mathbf{f}) \sqrt{\tilde{s}^m(\mathbf{f}) \tilde{s}^m(\mathbf{f})}, \quad (11)$$

where $\tilde{s}^m(\mathbf{f})$ is discretized PSD at node i , $\tilde{s}^m(\mathbf{f})$ is discretized PSD at node j , and Coh_{ij} is a coherence function between nodes i and j .

If auto-spectrum is assumed to be same for every location within the evaluated grid then $\tilde{s}^m(\mathbf{f}) = \tilde{s}^m(\mathbf{f})$ and the discretized cross spectral density between nodes i and j can be expressed as:

$$\tilde{s}^m(\mathbf{f}) = Coh_{ij}(\mathbf{f}) A_m \mathbf{f}^{-\frac{5}{3}} \delta f. \quad (12)$$

It is noted that tilde in the above equations represents the cross spectral density that gives the measure of the power of fluctuating velocity signal. This cross spectral density is later used to obtain amplitude of fluctuating velocity component by a combination of sine waves (Eq. (17)). Since amplitude of sine wave signal is twice the average signal power, Eq. (12) is modified as below in order to use the spectral density that maintain the set value of Tl :

$$S_{ij}^m(\mathbf{f}) = 2Coh_{ij}(\mathbf{f})A_m f^{-\frac{5}{3}}\delta f. \quad (13)$$

where $S_{ij}^m(\mathbf{f})$ is cross spectral density used to obtain correlated velocity amplitude.

Once the desired discretized cross spectral density is obtained from Eq. (13) for all mid-frequencies, velocity weighting factor $H(\mathbf{f})$ in frequency domain can be calculated using Cholesky's decomposition as suggested in [23]:

$$\begin{aligned} H_{11} &= S_{11}^{1/2}, \\ H_{21} &= S_{21}/H_{11}, \\ H_{22} &= (S_{22} - H_{21}^2)^{1/2}, \\ H_{31} &= S_{31}/H_{11}, \\ H_{jj} &= (S_{jj} - \sum_{l=1}^{l=j-1} H_{il}H_{jl})/H_{jj}, \\ H_{jj} &= (S_{jj} - \sum_{l=1}^{l=j-1} H_{jl}^2)^{1/2}, \end{aligned} \quad (14)$$

In the above equation, both $H(\mathbf{f})$ and $S_{ij}(\mathbf{f})$ are written as H and S_{ij} and the superscript m has been dropped from H and S for simplicity and clarity. However, it is noteworthy that Eq. (14) is valid for any direction and both H and S are functions of frequency. Furthermore, if R is the total number of spatial nodes, Eq. (14) gives square matrices of H that are $R \times R$ in size for each discrete frequency between f_{min} and f_{max} for each of the three directional components m .

2.2. Velocity as a function of time

The velocity weighting factor H from Eq. (14) is utilized in this section to develop analytical expressions for water velocity at each grid node as a function of time. A random phase angle θ_{ki} is associated with every frequency component f_k and every node i . Each of these random phase angles have an equal probability of occurrence between 0 and 2π . Using these phase angles and the weighting factor H , the amplitude of the fluctuating velocity component, m_{kj}^* , at node j can be written as a function of the frequency component f_k in a similar form to that suggested by [23]:

$$m_{kj}^* = \sum_{l=1}^j H_{lj}^m(f_k) e^{i\theta_{kl}}. \quad (15)$$

It is seen that Eq. (15) gives a complex value for $m_{kj}^* = |m_{kj}^*|e^{i\theta_{kj}^R}$, where θ_{kj}^R is a resultant phase angle for each frequency component at grid point j that accounts for the correlation with neighboring grid points according to:

$$\theta_{kj}^R = \tan^{-1} \left(\frac{\text{imag}(m_{kj}^*)}{\text{real}(m_{kj}^*)} \right), \quad (16)$$

where imag indicate imaginary part of m_{kj}^* and real indicates real part of m_{kj}^* .

Eq. (15) provides fluctuating velocity component contribution corresponding to each discrete frequency f_k . The total fluctuating velocity component m as a function of time at node j , is then obtained by treating the fluctuating contribution of each discrete frequency component as a sine wave and summing over k . In other words, velocity component $m_j(t)$ at node j for any instant of time t is obtained by:

$$m_j(t) = \sum_{k=1}^N |m_{kj}^*| \sin(2\pi f_k^* t + \theta_{kj}^R). \quad (17)$$

The fluctuating v and w components of velocity for each grid point, v_j and w_j , can be obtained directly using Eq. (17). Cross-axis correlation exists between the u , v and w components, but the effect of correlation is prominent only in the direction of flow (u component) [24]. Expressions to relate spectra of u , v and w components in integral form are available in [28] whereas the expressions to directly relate these components are found in [24]. The effective instantaneous fluctuating velocity in the direction of flow, $u_j^e(t)$, for node j can be given as suggested in [24]:

$$u_j^e(t) = u_j(t) + r_{uv}v_j(t) + 2r_{uw}w_j(t), \quad (18)$$

where r_{uv} is cross-axis correlation between u and v , r_{uw} is cross-axis correlation between u and w , and u_j is obtained from Eq. (17).

Expressions of r_{uv} and r_{uw} for ocean environments are not available, but these expressions exist for wind turbine [24] and have been adapted as below for the results presented in this paper:

$$r_{uv} = -0.136\sigma_u, \quad (19)$$

$$r_{uw} = -0.079\sigma_u - 0.325, \quad (20)$$

2.3. Turbulence integration in turbine simulation

The integration of the developed turbulence model into an existing OCT numerical simulation is presented in this section. This simulation is set to model an OCT with a 20 m diameter variable pitch 3 bladed rotor and uses the modeling approach presented by [21], with minor modifications presented in [20] that allow the effects of individual blade pitch to be simulated. XFOIL was used to calculate the lift and the drag. XFOIL does not allow for the effects of turbulence to be directly incorporated into the calculation of the lift and the drag coefficients but the Reynolds number utilized was 1,000,000. If the turbulence were directly accounted for, airfoil lift coefficient would increase as turbulence levels increase as shown by [29], resulting in increased power production values for higher ambient turbulence values. This simulation can be run as a 1 Degree Of Freedom (DOF) system to represent a bottom mounted turbine using a conventional foundation, with rotor rotation being the only allowed motion. It can also be run as a 7-DOF system (plus cable model degrees of freedom) where translation and rotation of turbine system about all axes are allowed, in addition to rotor rotation.

This numerical simulation approach uses an unsteady BEM rotor model for calculating the loadings on the rotor blades. A North East Down (NED) frame of reference with X-axis pointing north, Y-axis pointing east and Z-axis pointing downward in accordance with the right-hand-rule is used to integrate turbulence into the existing turbine simulation [20–21]. Two separate grids are utilized by this model, one for calculating a velocity deficit field and another for calculating the forces on the rotor blades. The grid used for calculating the velocity deficit field, referred as rotor grid, is defined by dividing the area swept by the rotor into evenly spaced annular and angular sections with respect to rotor radius and azimuth angle respectively. This is done to create a grid that travels with the turbine, but does not rotate with the rotor. This grid is used for calculating the velocity deficit, \mathbf{W}_o , resulting from the momentum that is extracted from the flow by the turbine. To calculate this velocity deficit at each rotor grid point, it is first assumed that there is a blade element at each grid point and that the lift force per unit length on each element is calculated using the motion of the turbine (including the rotor rotational speed), ambient water velocity at this grid point and velocity deficit at this grid point from the previous time step. This lift force is used to calculate a quasi-static velocity deficit vector, \mathbf{W}_{qs} , at each grid point, with components in the axial and tangential directions [30]. To take into account the time delay before the velocity deficit reaches its equilibrium values, a dynamic wake model consisting of two first order differential equations is numerically solved as suggested by [30]. Solving these numerically at each rotor grid point is accomplished using two intermediate wake variable vectors, \mathbf{H} and \mathbf{W}_{int} , with the wake deficit at each time step found according to [20]:

$$\mathbf{H} = \mathbf{W}_{qs}(n) + k\tau_1 \frac{\mathbf{W}_{qs}(n) - \mathbf{W}_{qs}(n-1)}{\Delta t} \quad (21)$$

$$\mathbf{W}_{int}(n) = \mathbf{H} + (\mathbf{W}_{int}(n-1) - \mathbf{H})e^{-\frac{\Delta t}{\tau_1}} \quad (22)$$

$$\mathbf{W}_o(n) = \mathbf{W}_{int}(n) + (\mathbf{W}_o(n-1) - \mathbf{W}_{int}(n))e^{-\frac{\Delta t}{\tau_2}}, \quad (23)$$

where τ_1 and τ_2 are time constants, n is the current time step number and Δt is the most recent time step size.

The velocity deficit vectors calculated using Eq. (23) are then used during the next time step to calculate the velocity deficit at the actual rotor blades. This is done by interpolating to find the velocity deficit values for each blade element on a blade grid (grid containing all blade elements) from the nearest rotor grid location as a function of rotor blade azimuth angle. Each impeded flow value is then converted from the axial and tangential directions into the NED reference frame and summed with the undisturbed flow velocity (Eq. (25)) and then blade velocity is subtracted to calculate the relative velocity of each blade element in the NED frame.

Forces are then calculated on each airfoil element using a blade element approach. These forces are calculated as a function of the relative water velocity, with the angle of attack of each blade element used to calculate the associated lift and drag coefficients each time step. The velocity magnitude and blade geometry are used to dimensionalize these coefficients. The net forces and moments on the rotor blade are then found using numerical integration. The extension of this numerical simulation [20–21] to include turbulence effects calculated using the method discussed in the preceding section is presented here.

The approach used in [20] to calculating the free-stream water velocity, \mathbf{V}^j , at each mesh node j (both the rotor and blade grid nodes) in the NED coordinate system includes two environmental parameters:

$$\mathbf{V}^j = \mathbf{V}_c^j + \mathbf{V}_w^j \quad (24)$$

where \mathbf{V}_c^j is current induced water velocity and \mathbf{V}_w^j is wave induced water velocity. To incorporate turbulence into this model, the turbulence induced water velocity, \mathbf{V}_t^j , is added to the water velocity induced by current shear and waves extending Eq. (24) to:

$$\mathbf{V}^j = \mathbf{V}_c^j + \mathbf{V}_w^j + \mathbf{V}_t^j \quad (25)$$

In this equation, \mathbf{V}_t^j is in the NED coordinates and both grids move with the turbine (one also rotating with the rotor). Conversely, the turbulence induced velocities calculated from Eqs. (17) and (18) are aligned with the flow, the grid is perpendicular to the flow, and the grid points remain stationary. To transform the turbulent water velocities from a frame aligned with the flow into NED coordinates, the mean flow angle with respect to North, ϕ , is utilized:

$$\mathbf{V}_{t,rotor}^j = \begin{bmatrix} \cos\phi & -\sin\phi & 0 \\ \sin\phi & \cos\phi & 0 \\ 0 & 0 & 1 \end{bmatrix} \begin{bmatrix} u_j^e \\ v_j \\ w_j \end{bmatrix} \quad (26)$$

where $\mathbf{V}_{t,rotor}^j$ is turbulent water velocities calculated in rotor grid in NED frame; and u_j^e , v_j and w_j are calculated from Eqs. (17) and (18).

Because the turbulence model does not directly calculate water velocities on the blade grid, but only on the rotor grid, linear interpolation is used calculate turbulence induced water velocity on the blade grid, $\mathbf{V}_{t,blade}^j$, as it rotates through the rotor grid. Because the technique used for calculating the components of turbulent velocity requires a fixed grid, these cannot be directly calculated using the presented model in this paper. The turbulent water velocities, \mathbf{V}_t^j , in Eq. (25) represents turbulent water velocities found for both of these grids.

The turbulence approach presented here assumes that the rotor plane containing nodes where turbulent velocities are simulated is perpendicular to the mean flow direction. For the moored turbine simulation, misalignment between flow direction and rotor grid will occur when the turbine pitches and yaws (see Fig. 8), creating small phase shifts in the sinusoidal velocity components for nodes that are up-stream or downstream from their assumed position. These phase shifts will create small inaccuracies in the simulated velocities at the associated grid points. However this misalignment is likely to be small as the plane of turbine is typically nearly normal to the direction of flow. In addition, the turbulence simulation approach assumes that the turbulence grid is fixed with respect to the earth, whereas the rotor grid is not fixed in the 7 DOF simulation which can lead to error. However, the motion of turbine, and in turn the motion of rotor grid, is small compared to water speed and therefore it is reasonable to neglect this error. For example, the maximum turbine velocity calculated from the simulations carried out in this study occurred for $TI = 20\%$ and was 0.3 m/s, whereas the mean water speed was 1.6 m/s.

3. Results

3.1. Turbulent flow field

Numerical simulations are run to evaluate the temporal and spatial water velocity variability using the method discussed above. Time histories for a single point are presented to display the temporal variability of the water velocity, velocity spectra show that the desired spectra are accurately modeled, and instantaneous water velocities over the swept area of the rotor are presented to show the spatial variability. Simulations are run with $\bar{U} = 1.6$ m/s, $f_{min} = 0.01$ Hz, $f_{max} = 1$ Hz and frequency discretization of 1501 points i.e. 1500 mid-frequency points. Values of P and Q equal to 0.8 and 0.5 respectively are utilized in these simulations.

Temporal variability is evaluated for $TI = 5\%$ and 20% using simulation run times of 3600 s. Although TI is site specific, measurements at potential tidal energy production sites in USA and Chile have measured TIs that vary between 5% and 20% with velocity data processed in 5 min burst after removing Doppler's noise [31] so results for these TIs are presented. Fig. 1 shows velocity time histories at one of the nodes on a circular grid for $TI = 5\%$ and 20% . The time averaged velocities in the flow direction (Figs. 1a and 1b) are calculated to be $\bar{U} = 1.6$ m/s for both TIs . Figs. 1c and 1d show velocity time histories in cross stream and vertical direction for $TI = 5\%$ and 20% . The mean velocities \bar{v} and w obtained from simulation are nearly equal to 0 (e.g. 0.00005 and -0.00014 respectively for $TI = 5\%$). Table 1 shows simulation results as well as input standard deviations calculated from Eq. (4) and the relations $\sigma_v = P\sigma_u$ and $\sigma_w = Q\sigma_u$ for both TI cases. It is seen that TIs obtained from simulations are within 0.32% of input values. It may be noted that longer simulated time histories and higher number of frequency discretization reduces the differences between calculated parameters from equations and simulation.

Velocity time series for $TI = 5\%$ calculated at a single node are reconstructed back to frequency domain (Fig. 2) in order to examine the recovery of 5/3 input spectra and a value of $C = 5$ is utilized. Convergence of the reconstructed spectra are examined for mid-frequency discretization (N) of 300, 1500 and 3000. Velocity spectra of u , v and w velocity components are shown for simulation time of 3600 s (Fig. 2, top) and 5400 s (Fig. 2, bottom). It is seen that simulation time longer than 3600 s only minimally increases the convergence of velocity spectra. It is also observed that the reconstructed spectra is

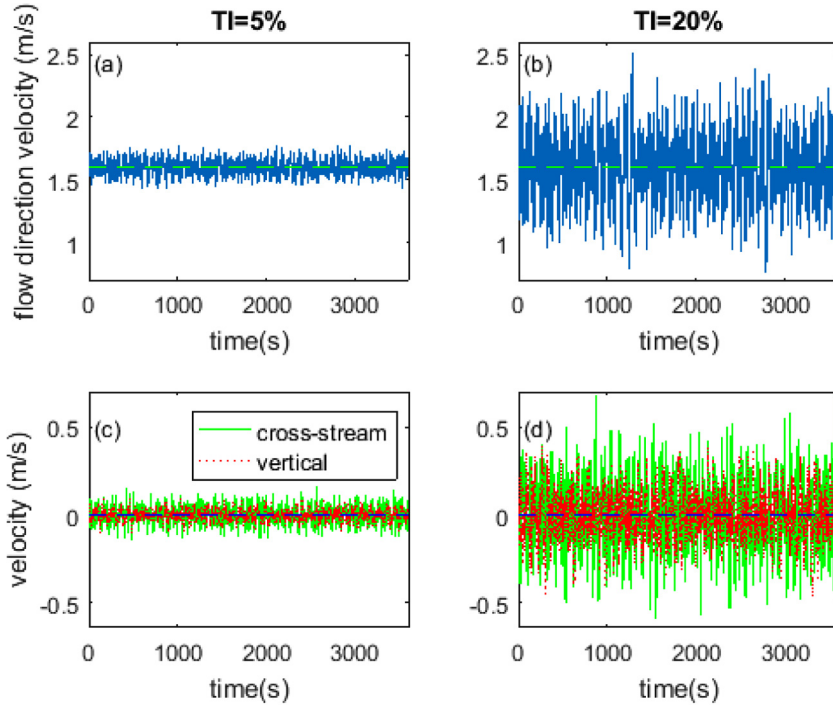


Fig. 1. Water velocity time histories in all three directions for turbulence intensities of 5% and 20%.

Table 1
Comparison of input and simulated standard deviations and turbulence intensities

$TI = 5\%$		$TI = 20\%$	
Input (m/s)	Simulation (m/s)	Input (m/s)	Simulation (m/s)
σ_u	0.058	0.059	0.233
σ_v	0.047	0.051	0.186
σ_w	0.029	0.029	0.116
TI	5.00%	5.20%	20.00%

noisy and less accurate for $N = 300$, whereas these reconstructed spectra are almost identical to the input 5/3 line for $N = 1500$ and 3000. Since the simulation with time of 3600 s and $N = 1500$ have reproduced the input 5/3 spectra with relatively high accuracy (see Fig. 2), these values are utilized in the turbine simulations presented in this paper.

Spatial variability figures are presented to demonstrate how flow correlation effects the flow field over the rotor area. Fig. 3 shows velocity plots in the direction of flow on a circular grid with azimuthal angles discretized to 8 equal parts and radius of circle discretized to 5 equal parts. These figures are for an instantaneous time of $t = 5\text{s}$ and a $TI = 5\%$ for $C = 2$ (Fig. 3a) and 27 (Fig. 3b). This circular grid represents a 10 m rotor radius where the color scale indicates the instantaneous velocities throughout the rotor swept area due to turbulence.

Velocities over the grid are more uniform in Fig. 3a where $C = 2$ compared to Fig. 3b where $C = 27$. This is because a higher magnitude of C reduces the correlation between velocities at different nodes. Therefore, C can be chosen based on the degree of correlation observed different ocean sites. For wind turbines, values of C ranging from 2 to 27 have been suggested [23]. It is noteworthy that the value of C only affects velocity correlation between nodes, and does not affect standard deviations calculated from velocity time histories.

3.2. Turbulence effects on turbine

The turbulent flow modeling approach presented in this paper is integrated into the numerical simulation of OCT developed by [20] [21] as discussed in Section 2.3. Simulations are run for the 1-DOF system that represents a fixed tidal turbine and the 7-DOF system that represents an OCT with compliant mooring system. Prototype turbines will likely be tested using mooring systems that allow for relatively quick OCT deployment and retrieval, such as the mooring system shown in Fig. 4. However, in a commercial array is likely that OCTs will be attached to mooring cables that are directly anchored to see floor. For the 7-DOF simulation results presented in this paper, a mooring system similar to the one presented in Fig. 4 is assumed.

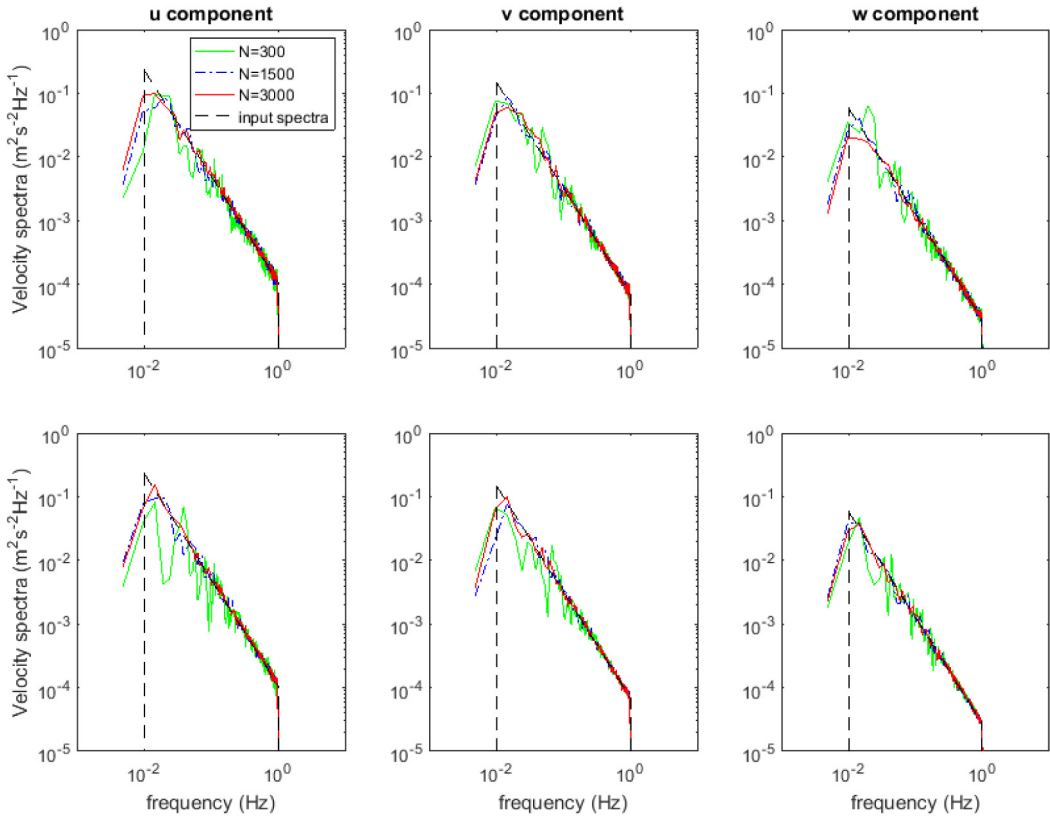


Fig. 2. Velocity spectra reconstructed from numerical simulation generated time histories using “ N ” frequency components for simulation times of 3600 s (TOP) AND 5400 s (BOTTOM).

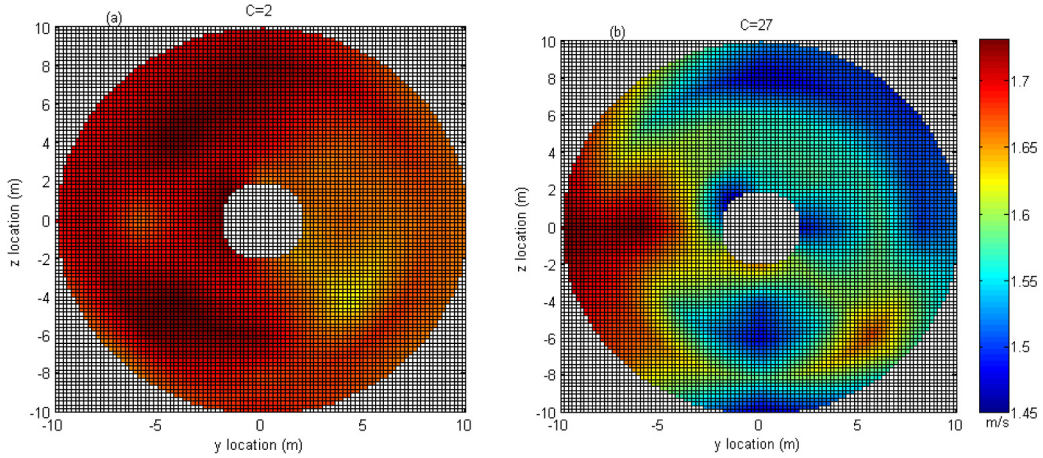


Fig. 3. Velocity in the streamwise direction at an instantaneous time for $C = 2$ (a) and $C = 27$ (b).

For computational efficiency only the OCT (Turbine Generator) and the horizontal line that attaches this OCT to the main mooring cable are numerically modeled. The effects of ocean waves are not taken into account in these simulations to solely evaluate the impacts of turbulence. Fluctuation of hydrodynamic parameters including as shaft power, torque and axial loading on one blade are presented in both the time and frequency domain. Additionally, effects of turbulence on Euler angles are evaluated for the compliantly mooring system.

Fig. 5 shows time histories of shaft power and hydrodynamic torque for mean flow speed of 1.6 m/s, $C = 5$, $f_{min} = 0.01$ Hz, $f_{max} = 1$ Hz and $TIs = 5\%$ and 20% for one hour 1-DOF (Fig. 5 top) and 7-DOF (Fig. 5 bottom) simulations. The simulations are run at constant rpm of 15.49 that maintain optimal tip speed ratio.

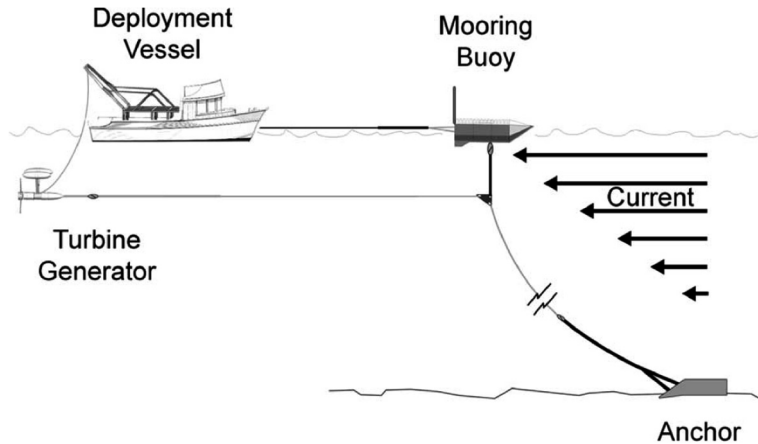


Fig. 4. Representation of a potential mooring system for testing prototype octs. please note that the mooring cables are not drawn to scale.

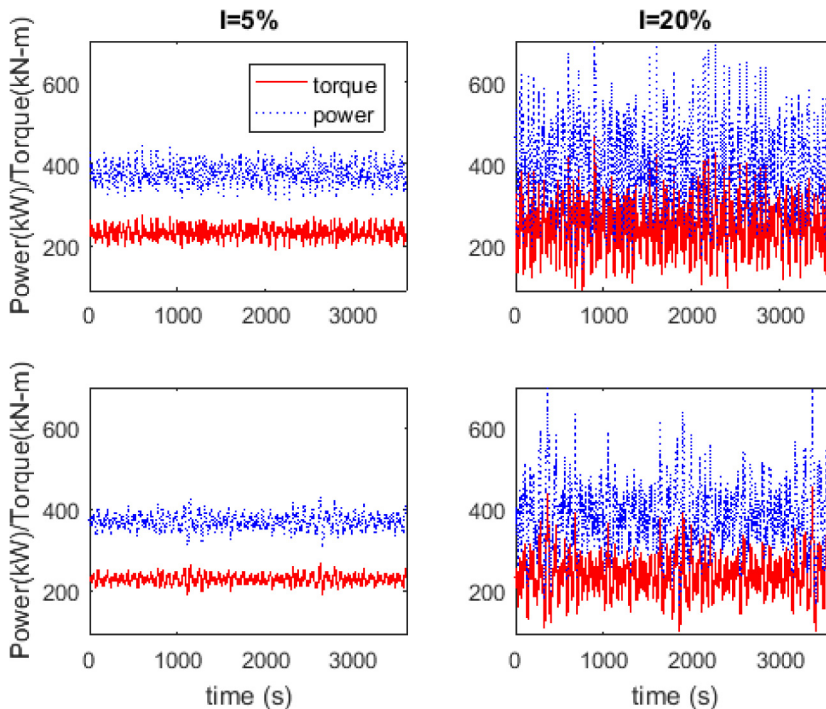


Fig. 5. Shaft power and hydrodynamic torque for 1 dof (TOP) and 7 dof (bottom) simulations run at 5% (left) and 20% (right) turbulence intensities.

For 1-DOF system, mean shaft power and hydrodynamic torque for $TI = 5\%$ are 375.8 kW and 231.6 kN.m respectively. It can be observed from Fig. 5 (top left) that power and hydrodynamic torque have total fluctuations, i.e. difference between maximum and minimum values, of 135 kW and 83 kN.m for $TI = 5\%$. The standard deviations of shaft power and torque are 23.14 kW and 14.26 kN.m for this TI . This result indicates that even for locations where turbulence levels are relatively low, $TI = 5\%$, its effects on turbine performance are strong and should not be neglected. Similarly, for $TI = 20\%$, (Fig. 5, top right) mean shaft power and hydrodynamic torque are 393.0 kW and 242.3 kN.m. Likewise, the standard deviations of shaft power and hydrodynamic torque are 91.6 kW and 56.5 kN.m. $TI = 20\%$ represents a high turbulence scenario where turbine performance can vary greatly, requiring control system to minimize power and torque fluctuations. Overall, it can be seen in Fig. 5 that mean values of torque and power are slightly greater for $TI = 20\%$ than for $TI = 5\%$, while the standard deviations of these parameters are about 4 times higher for $TI = 20\%$ than for $TI = 5\%$. Higher standard deviation of power for higher TI is both intuitive and has been documented in previous study [27]. Similarly, slight increases in average power with increases in TI have also been noted [32].

For the 7-DOF system, mean shaft power and hydrodynamic torque for $TI = 5\%$ (Fig. 5, bottom left) are about 370 kW and 228 kN.m respectively whereas these values are 384.2 kW and 236.8 kN.m for $TI = 20\%$ (Fig. 5, bottom right). The mean

powers for 7-DOF cases are 1.5% and 2.2% less than the powers for 1-DOF cases for TI of 5% and 20% respectively. This is likely due to slight misalignment between rotor planes and the mean flow velocities (Euler angles) for 7-DOF case and also because of motion of entire turbine system. Standard deviations of power for $TI = 5\%$ and 20% are about 17.2 kW and 74.6 kW respectively.

Fig. 6 (top) shows axial force variation in 1-DOF system for one blade of the tri-bladed rotor for $TI = 5\%$ and 20%. The mean force for $TI = 5\%$ is 139.2 kN, with a standard deviation of 3.7 kN. Similarly, for $TI = 20\%$ the mean force is 140.3 kN, with a standard deviation of 14.4 kN. It is observed that while the mean force is only 0.79% higher for $TI = 20\%$, the standard deviation is 3.89 times higher. This shows that fatigue load can be a major cause of blade damage if a turbine is operating under extreme turbulence.

Fig. 6 (bottom) shows axial force on one blade of the tri-bladed rotor for 7-DOF system. Mean forces for $TI = 5\%$ and 20% are 139 kN and 140 kN, with standard deviations of 3 kN and 12 kN respectively. Although these mean axial force values are almost same (only low by 0.14% and 0.21% for TIs of 5% and 20%) as 1-DOF case, their standard deviations are significantly lower by 18.9% and 16.6% than 1-DOF case for TIs of 5% and 20%.

Fig. 7 shows the Power Spectral Density (PSD) of shaft power and axial force on the rotor for 1-DOF and 7-DOF systems operating in $TI = 5\%$. The dashed straight lines represent lines that follow five thirds power of frequency. It can be seen that overall variance (area under the PSD curve) is higher for 1-DOF system compared to 7-DOF system, which indicate that a moored (7-DOF case) turbine experiences a more consistent power production and lower fatigue loads than a fixed (1-DOF case) turbine for this operating condition. This is likely because the compliance in this mooring system reduces peaks and troughs in the relative water velocity caused by turbulence, and thus extreme (both minimum and maximum) power and loading scenarios. Major peaks are observed in PSD of axial force for both 1 and 7-DOF systems (**Fig. 7** right). For 1-DOF system the peak is observed at a frequency of approximately 0.25 Hz, which is the frequency of rotor rotation. The primary peak for 7-DOF system at about 0.055 Hz is likely due to the natural frequency of moored cable system.

Fig. 8 shows time histories of the Euler angles of turbine system for the moored OCT (7-DOF system). For $TI = 5\%$, fluctuation ranges of 0.87°, 0.58° and 2.1° are found in roll, pitch and yaw respectively; whereas these corresponding ranges for $TI = 20\%$ are 4.3°, 2.1° and 11.51°. It is noted that yaw is most sensitive to turbulence level. Also, a peak at frequency of about 0.04 Hz was noted in a PSD of roll (not shown here). This is likely due to the natural roll frequency of this system associated with the separation between the center of gravity and center of buoyancy.

The displacement from equilibrium position of turbine system is found to be significantly affected by turbulence at mean water speed of 1.6 m/s. The maximum periodic displacement in along flow direction is found to be 5.5 m for $TI = 20\%$. Similarly, at this TI , the maximum periodic displacement in cross-stream and down directions are 5.5 and 5.2 m. The results suggest that for the evaluated frequency range, turbulence effect is important for not only shaft power and blade loading, but also for overall motion of turbine system.

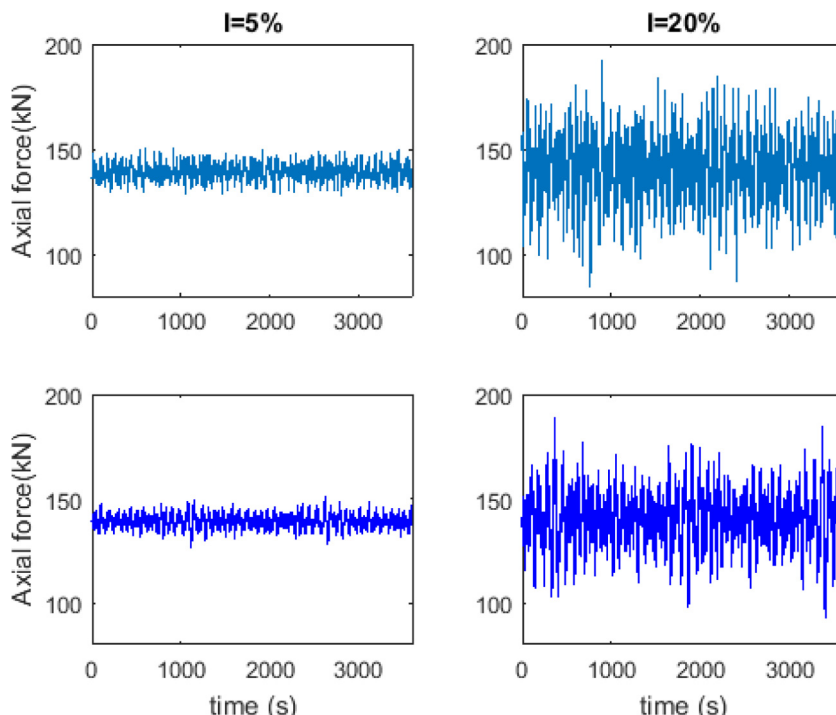


Fig. 6. Axial force on a single rotor blade for 1 dof (top) and 7-dof (bottom) simulations run AT 5% (left) and 20% (right) turbulence intensities.

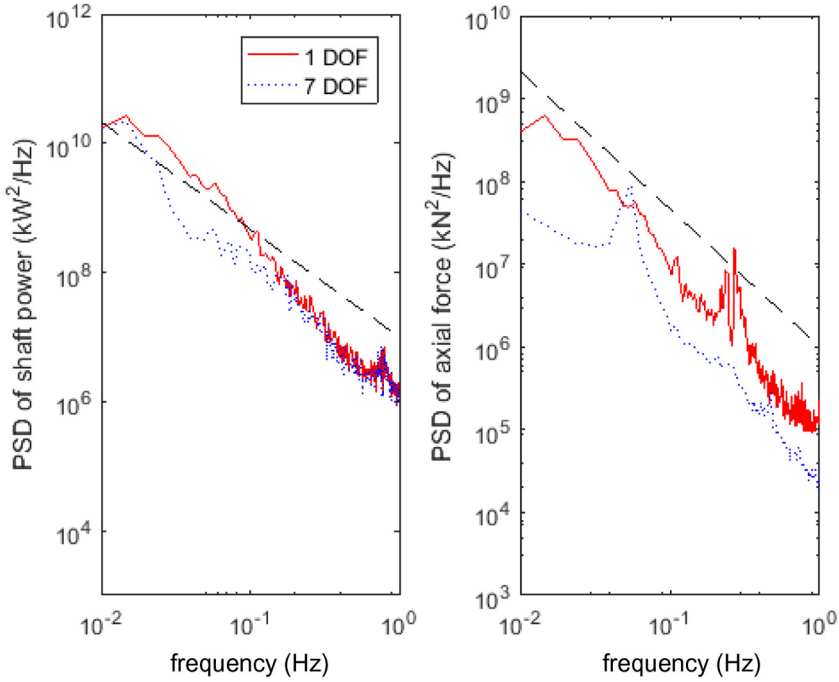


Fig. 7. PSD for shaft power (left) And axial force (right) for $TI = 5\%$ with the dashed lines showing representative 5/3 lines.

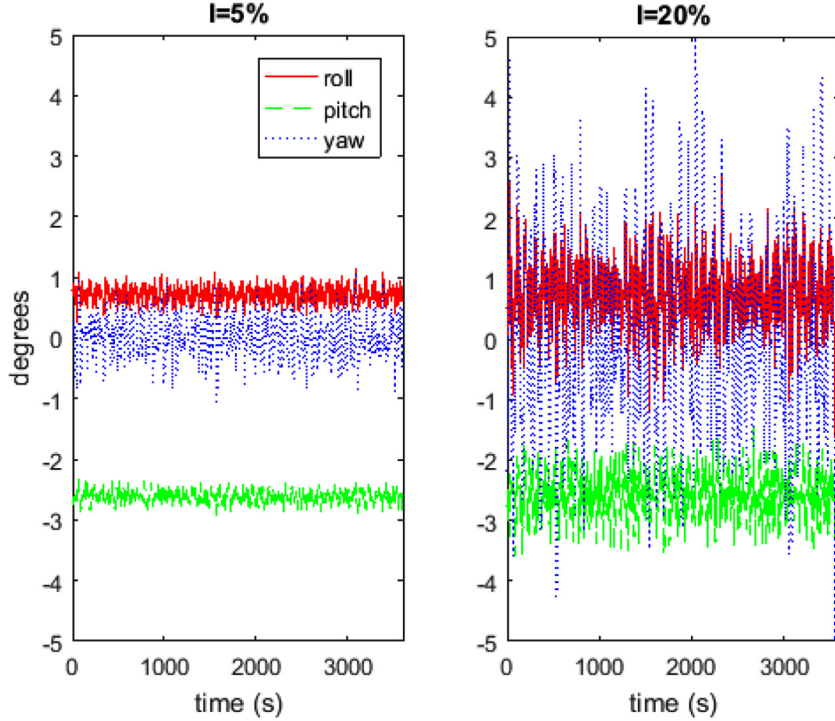


Fig. 8. Euler angles for turbine system with 7 dof for $TI = 5\%$ (left) and 20% (right).

3.3. Sensitivity analysis

Intense coherent turbulent structures have been seen in natural wind flow which have caused large cyclical load on wind turbine [33]. These turbulent structures also likely exist in ocean environment. Therefore, to evaluate the impact of high flow

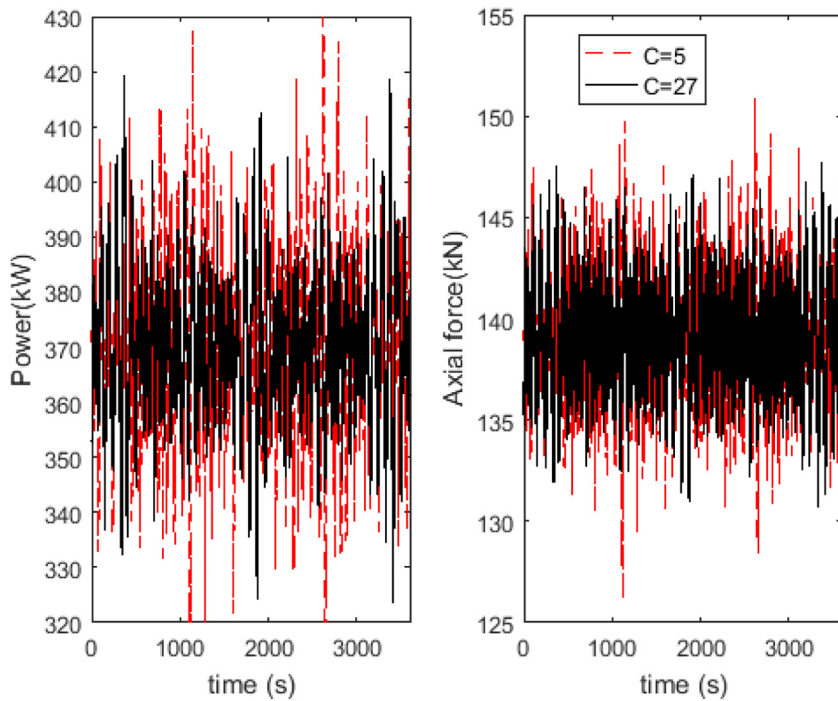


Fig. 9. Effects of flow correlation on shaft power (left) and hydrodynamic axial force on the rotor (right).

Table 2
Comparison of shaft power and hydrodynamic axial force on the rotor for different C values

	C = 5	C = 27
Mean power (kW)	369.99	370.04
Mean Axial force (kN)	139.08	139.07
Power standard deviation (kW)	17.28	12.75
Axial force standard deviation (kN)	2.96	2.38

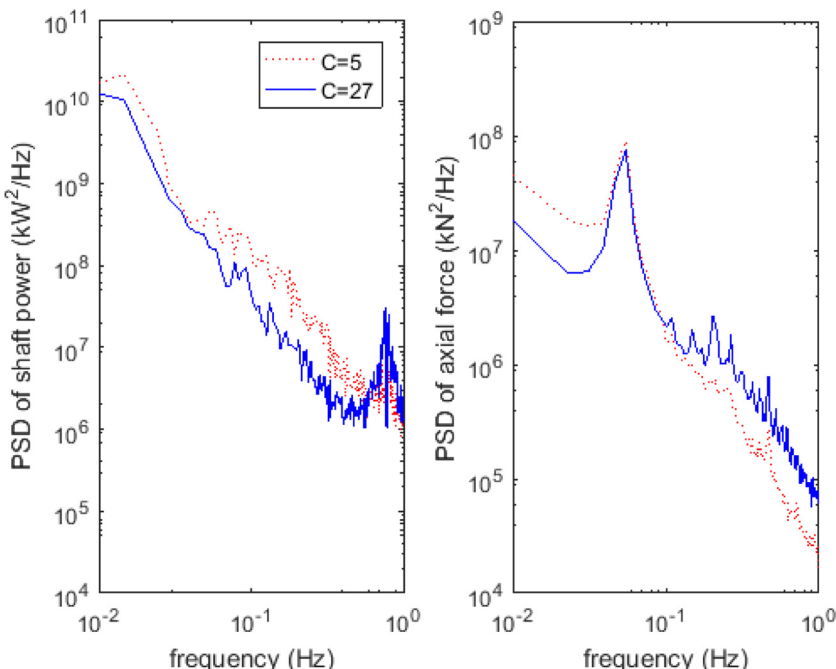


Fig. 10. Power (left) and hydrodynamic axial force (right) spectra for different flow correlations.

coherence on the compliant mooring OCT system, the value of coherence decay constant, C , is varied while keeping TI constant for 7-DOF simulation. It is noteworthy that lowering the value of C increases flow coherence.

Fig. 9 compares a highly coherent flow with $C = 5$ to a low coherence flow with $C = 27$ for $TI = 5\%$. It is seen that both the temporal fluctuations of axial force on one blade and shaft power get higher as velocity coherence increases, while mean values of these parameters do not change significantly (**Table 2**). Since TI is constant at 5%, temporal variability of velocities are same for both values of C . Hence, the temporal fluctuations of power and axial force are caused by spatial variability of velocities for different flow correlations (different C values). Higher correlation reduces the spatial velocity variability that causes flow field throughout rotor area to be uniform. This results in larger changes in flow field throughout rotor area per time step to ensure a constant value of TI and consequently, highly coherent flows cause more fatigue load on turbine blades as compared to flow with low correlation.

Fig. 10 shows the PSD of shaft power and axial force on one blade of tri-bladed rotor for both $C = 5$ and $C = 27$. It can be seen that shaft power is more variable over most of the spectrum for the higher coherence value i.e. $C = 5$ than for the case where flow coherence is low i.e. $C = 27$. This is true up to frequencies around 0.5 Hz, above which the less coherent flow produces a greater variance in shaft power. Similar results are seen for the axial force (**Fig. 10** right), except that the lower coherence results in more energetic loading scenario starting at a frequency above 0.09 Hz. Furthermore, similar peaks are seen for PSDs of axial force for both coherence at about same frequency. As previously mentioned, this peak is likely due to the natural frequency of a moored OCT system.

4. Conclusions

An approach for calculating turbulent flow velocity without having to generate velocity time history is described. The approach is integrated in a numerical simulation of an OCT for predicting loadings and system response in an oceanic environment. It is shown that turbulence can have significant impact on power production, as well as the loading on this turbine. Although time averaged mean values of power and axial loading on a blade do not change substantially with change in ambient turbulence intensities, the standard deviations of power and axial loading increase by 3.9 and 3.8 times when turbulence intensity is increased from 5% to 20% for a bottom mounted turbine (1-DOF case). Similar results are found for a moored turbine (7-DOF case), with increases of 4.3 and 4 times respectively. Higher flow correlation is found to increase fluctuations in axial blade loading, as well as power for the same value of ambient turbulence intensity up to frequencies of 0.09 and 0.5 Hz respectively for a moored OCT.

Acknowledgements

This material is based upon work supported by the National Science Foundation under Grant No. ECCS-1307889. SNMREC is supported by the U.S. Department of Energy and the State of Florida.

References

- [1] BOEM, "Ocean Current Energy," Bureau of Ocean Energy Management, <<http://www.boem.gov/Renewable-Energy-Program/Renewable-Energy-Guide/Ocean-Current-Energy.aspx>> (accessed 28.01. 16).
- [2] HYCOM, Consortium for Data Assimilative Modeling [Online]. Available: <<http://hycom.org/>>, 2012.
- [3] J.H. Van Zwieten Jr., A.E.S. Duerr, G.M. Alsenas, H.P. Hanson, Global ocean current energy assessment: an initial look, in: Proceedings of the 1st Marine Energy Technology Symposium (METS13) hosted by the 6th annual Global Marine Renewable Energy Conference, April 10–11, Washington D.C. 2013. Available: <<http://www.forceanenergy.org/mets/2013-peer-reviewed-mets-papers/>>.
- [4] GeorgiaTech Research Corp., Assessment of Energy Production Potential from Ocean Currents along the United States Coastline, Atlanta, GA, 2013.
- [5] U.S. Energy Information Administration, 2015, "Annual Energy Review," <<http://www.eia.gov/>>.
- [6] M.C.P.M. Machado, J.H. Van Zwieten, I. Pinos, A measurement based analyses of the hydrokinetic energy in the gulf stream, *J. Ocean Wind Energy* 3 (1) (2016) 25–30.
- [7] J. Van Zwieten, W. McAnalley, J. Ahmad, T. Davis, J. Martin, M. Bevelhimer, A. Cribbs, R. Lippert, T. Hudon, M. Trudeau, In-stream hydrokinetic power – a review and appraisal, *J. Energy Eng.* 2014, no. 04014024.
- [8] K. Kubo, Y. Kubata, K. Nakamura, S. Nagaya, T. Ueno, T., Development of blade for floating type current turbine system, Oceans – St. John's, 2014.
- [9] I.A. Milne, R.N. Sharma, R.G.J. Flay, S. Bickerton, The role of onset turbulence on tidal turbine blade loads, in: 17th Australasian Fluid Mechanics Conference, Auckland, New Zealand, 5–9 December 2010.
- [10] P. Mycek, B. Gaurier, G. Germain, G. Pinon, E. Rivoal, Experimental study of the turbulence intensity effects on marine current turbines behaviour. Part I: one single turbine, *Renewable Energy* 66 (2014) 729–746.
- [11] T. Blackmore, W.M.J. Batten, A.S. Bahaj, Influence of turbulence on the wake of a marine current turbine simulator, *Philosophical Transactions A, The Royal Society Publishing*, 2014.
- [12] N.D. Kelley, B.J. Jonkman, Overview of the TurbSim Stochastic Inflow Turbulence Simulator, National Renewable Energy Laboratory, 2005.
- [13] B. Jonkman, L. Kilcher, TurbSim User's Guide: Version 1.06.00, NREL, 2012.
- [14] R.J. Cavagnaro, Impact of Turbulence on the Control of a Hydrokinetic Turbine, International Conference on Ocean Energy, Canada, 2014.
- [15] J. Thomson, B. Polagye, V. Durgesh, M.C. Richmond, Measurements of Turbulence at Two Tidal Energy Sites in Puget Sound, WA, *IEEE J. Oceanic Eng.* 37 (3) (2012).
- [16] P. Bradshaw, Conditions for the Existence of an Inertial Subrange in Turbulent Flow, in: Reports and Memoranda No. 3603, Aeronautical Research Council, London, 1969.
- [17] R.W. Johnson, *The Handbook of Fluid Dynamics*, CRC Press and Springer, 1998, ISBN 3-540-64612-4.
- [18] J.R. Chasnov, Simulation of the Kolmogorov inertial subrange using an improved subgrid model, *Phys. Fluid* 3 (1) (1991) 188–200.
- [19] T. Blackmore, L.E. Myers, A.S. Bahaj, Effects of turbulence on tidal turbines: implications to performance, blade loads, and condition monitoring, *Int. J. Mar. Energy* 14 (2016) 1–26.

- [20] J.H. VanZwieten Jr, N. Vanrietvelde, B.L. Hacker, Numerical simulation of an experimental ocean current turbine, *IEEE J. Oceanic Eng.* 38 (1) (2013) 131–143.
- [21] J.H. VanZwieten, P. Pyakurel, T. Ngo, C. Sultan, N.I. Xiros, An assessment of using variable blade pitch for moored ocean current turbine flight control, *Int. J. Mar. Energy* 13 (2016) 16–26.
- [22] T. Nevalainen, C. Johnstone, A. Grant, A., Quasi unsteady blade element momentum theory for tidal stream turbines, 3rd Oxford Tidal Energy Workshop 7–8 April 2014, Oxford, UK, 2014.
- [23] P.S. Veers, *Three-Dimensional Wind Simulation*, Sandia National Laboratories, 1988.
- [24] N.D. Kelley, *Full Vector (3-D) Inflow Simulation in Natural and Wind Farm Environments using an Expanded Version of the SNLWIND (VEERS) Turbulence Code*, NREL, 1992.
- [25] P. Pyakurel, J.H. VanZwieten, P. Ananthakrishnan, W. Tian, Simulating turbulence for ocean current turbine, in: 21st SNAME Offshore Symposium, Houston, February 2016.
- [26] J.C.R. Hunt, J.C. Vassilicos, Kolmogorov's Contributions to the Physical and Geometrical Understanding of Small-Scale Turbulence and Recent Developments, in: Royal Society Publishing, Proceedings: Mathematical and Physical Sciences, Vol. 434, No. 1890, Turbulence and Stochastic Process: Kolmogorov's Ideas 50 Years On, Jul. 8, 1991, pp. 183–210.
- [27] F. Maganga, G. Germain, J. King, G. Pinon, E. Rivoalen, Experimental characterisation of flow effects on marine current turbine behaviour and on its wake properties, *IET Renewable Power Gener.* 4 (6) (2010) 498–509.
- [28] H. Nakagawa, I. Nezu, *Turbulence in Open Channel Flows*, Taylor & Francis, 1993.
- [29] J.A. Hoffmann, Effects of freestream turbulence on the performance characteristics of an airfoil, *AIAA J.* 29 (9) (1991) 1353–1354.
- [30] M.O.L. Hansen, *Aerodynamics of Wind Turbines*, Earthscan, London, UK, 2008, pp. 85–100.
- [31] J. Thomson, L. Kilcher, M. Richmond, J. Talbert, A. deKlerk, B. Polagye, M. Guerra, R. Cienfuegos, Tidal turbulence spectra from a compliance mooring, in: Proceedings of the 1st Marine Energy Technology Symposium, METS2013, April 10–11, 2013, Washington, D.C.
- [32] Q. Li, Y. Kamada, T. Maeda, J. Murata, N. Yusuke, Effect of turbulence on power performance of a Horizontal Axis Wind Turbine in yawed and no-yawed flow conditions, *Energy* 109 (2016) 703–711.
- [33] N.D. Kelley, *Turbulence-Turbine Interaction: The Basis for the Development of the TurbSim Stochastic Simulator*, National Renewable Energy Laboratory (NREL), 2011.